Ocean Sci. Discuss., 11, 1643–1689, 2014
www.ocean-sci-discuss.net/11/1643/2014/
doi:10.5194/osd-11-1643-2014


Ocean Science
Discussions
Open Access



# Measuring air–sea gas exchange velocities in a large scale annular wind-wave tank

**E. Mesarchaki[1], C. Kräuter[2], K. E. Krall[2], M. Bopp[2], F. Helleis[1], J. Williams[1], and B. Jähne[2,3]**

[1]Max-Planck-Institut für Chemie (Otto-Hahn-Institut), Hahn-Meitner-Weg 1, 55128 Mainz, Germany
[2]Institut für Umweltphysik, Im Neuenheimer Feld 229, 69120 Heidelberg, Germany
[3]Heidelberg Collaboratory for Image Processing (HCI), Universität Heidelberg, Speyerer Straße 6, 69115 Heidelberg, Germany

Received: 1 May 2014 – Accepted: 5 June 2014 – Published: 23 June 2014

Correspondence to: E. Mesarchaki (evridiki.mesarchaki@mpic.de)

Published by Copernicus Publications on behalf of the European Geosciences Union.







## Abstract

In this study we present gas exchange measurements conducted in a large scale wind-wave tank. Fourteen chemical species spanning a wide range of solubility (dimensionless solubility, $\alpha = 0.4$ to 5470) and diffusivity (Schmidt number in water, $Sc_w = 594$ to 1194) were examined under various turbulent ($u_{10} = 0.8$ to $15\,m\,s^{-1}$) conditions. Additional experiments were performed under different surfactant modulated (two different concentration levels of Triton X-100) surface states. This paper details the complete methodology, experimental procedure and instrumentation used to derive the total transfer velocity for all examined tracers. The results presented here demonstrate the efficacy of the proposed method, and the derived gas exchange velocities are shown to be comparable to previous investigations. The gas transfer behaviour is exemplified by contrasting two species at the two solubility extremes, namely nitrous oxide ($N_2O$) and methanol ($CH_3OH$). Interestingly, a strong transfer velocity reduction (up to a factor of three) was observed for $N_2O$ under a surfactant covered water surface. In contrast, the surfactant affected $CH_3OH$, the high solubility tracer only weakly.

## 1 Introduction

The world's oceans are key sources and sinks in the global budgets of numerous atmospherically important trace gases, in particular $CO_2$, $N_2O$ and volatile organic compounds (VOCs) (Field et al., 1998; Williams et al., 2004; Millet et al., 2008, 2010; Carpenter et al., 2012). Gas exchange between the ocean and the atmosphere is therefore a significant conduit within global biogeochemical cycles. Air–sea gas fluxes, provided either by direct flux measurements or accurate gas transfer parameterizations, are a prerequisite for global climate models tasked to deliver accurate future predictions (Pozzer et al., 2006; Saltzman, 2009).

The principles behind gas exchange at the air–sea interface have been reported in detail within previous reviews (Jähne and Haussecker, 1998; Donelan and Wanninkhof,





OSD
11, 1643–1689, 2014



2002; Wanninkhof et al., 2009; Jähne, 2009; Nightingale, 2009). A simplified conceptual model is generally accepted whereby mass boundary layers are formed on both sides of the interface. The transport of gases across the boundary layers is controlled by molecular motion, expressed by the diffusion coefficient $D$. The transfer velocity $k$ (in $\mathrm{cm\,h^{-1}}$), of a gas across the surface is defined as the gas flux density $F$, divided by the concentration difference $\Delta c$, between air and water (henceforth named $k_t$ expressing the transfer through both boundary layers against the single air and water layer transfer, $k_a$ and $k_w$, accordingly). Wind driven turbulence near the water surface (surface stress and roughness, waves, breaking waves, bubbles, spray etc.), influences the thickness of the mass boundary layers. Thus, the transfer velocity is related to the degree of turbulence on both sides close to the interface as well as the tracer characteristics i.e., their solubility and diffusion coefficients (Danckwerts, 1951; Liss and Slater, 1974). The impact of wind driven mechanisms and diverse physiochemical tracer characteristics on the gas exchange rates can be studied in detail through transfer velocity measurements of individual species provided by the method proposed here. Such studies aim to cover poorly understood air–sea gas transfer regimes, provide direct tests for individual species and new insights into the theoretical background.

Gas transfer velocities have been determined in both field studies (using mass balance, eddy correlation or controlled flux techniques) and laboratory experiments described in previous gas exchange reviews (Jähne and Haussecker, 1998; Donelan and Wanninkhof, 2002; Wanninkhof et al., 2009; Jähne, 2009; Nightingale, 2009) and references therein. Wind-wave tanks, in contrast with the open ocean, offer a unique environment for the investigation of individual mechanisms related to the air–sea gas exchange under controlled conditions.

Mass balance methods have been applied in the field using geochemical tracers ($O_2$, $^{14}C$, Radon, for instance in Broecker et al., 1985) and dual tracer ($SF_6$, $^3He$, for instance in Watson et al., 1991; Wanninkhof et al., 1993) techniques. The main drawback of these approaches was the temporal resolution which led to time constants in the order of days to weeks. The measurement frequency was too low to probe the





OSD
11, 1643–1689, 2014



fast variability of the physical parameters controlling the gas exchange (Jähne and Haussecker, 1998). Furthermore, the transfer velocity measurements were based primarily on sparingly soluble tracers, and very few experimental results of highly soluble trace gas transfer velocities are available.

In this study, gas-exchange experiments were performed in a state-of-the-art large scale annular wind-wave tank. An experimental approach based on mass balance has been developed, whereby air and water side concentrations of various tracers are monitored using instrumentation capable of on-line measurement. For the first time, parallel measurements of total air and water-side transfer velocities for 14 individual gases within a wide range of solubility, have been achieved. Wind speed conditions (reported at ten meters height, $u_{10}$) as low as 0.8 reaching up to 15 m s$^{-1}$ were investigated. Supplementary parameters directly linked with the gas exchange velocities, such as friction velocity and mean square slope of the water surface, were additionally measured under the same conditions. This paper details the entire instrumental set-up and provides a validation of the overall operation and concept through transfer velocity measurements of nitrous oxide and methanol. These species are chosen as they bracket the wide range of solubilities among the investigated tracers and show clearly different gas exchange behaviours.

## 2 Method

In this study, total transfer velocities for low as well as medium to highly soluble tracers were determined using a mass balance approach. The wind-wave tank is interpreted in terms of a box model.





OSD
11, 1643–1689, 2014



## 2.1 The box model

The basic idea of the box model method is the development of a direct correlation between the air and water-phase concentrations, $c_a$ and $c_w$, and the desired transfer rates $k_t$ of various tracers.

Figure 1 shows a schematic representation of the wind-wave tank in a box model (Kräuter, 2011; Krall, 2013). Water and air-spaces are assumed to be two well-mixed separate boxes, $V_w$ and $V_a$ between which tracers can be exchanged only through the water surface, $A$. Further possible pathways of tracers entering or leaving the box are also shown in Fig. 1. Assuming constant volumes, temperature and pressure conditions, the mass balance for the air and the water phases of the box yields for a water-side perspective:

$$V_a \dot{c}_a = A k_{tw}(c_w - \alpha c_a) + \dot{V}_a^i c_a^i - \dot{V}_a c_a + \dot{V}_a c_a^0 \quad (1)$$

$$V_w \dot{c}_w = -A k_{tw}(c_w - \alpha c_a) \quad (2)$$

and an air-side perspective:

$$V_a \dot{c}_a = -A k_{ta}\left(c_a - \frac{c_w}{\alpha}\right) + \dot{V}_a^i c_a^i - \dot{V}_a c_a + \dot{V}_a c_a^0 \quad (3)$$

$$V_w \dot{c}_w = A k_{ta}\left(c_a - \frac{c_w}{\alpha}\right), \quad (4)$$

where $\alpha = c_w/c_a$, denotes the dimensionless solubility and $k_{tw}$, $k_{ta}$ the total transfer velocities for a water and an air-sided viewer, respectively. The two transfer velocities differ by the solubility factor of the tracer (see Eq. A1).

The first term on the right hand side of each equation represents the exchange of a tracer from one phase to the other due to a concentration gradient. The second term stands for possible tracer input ($\dot{V}_a^i c_a^i$), the third term for possible tracer output (flushing/leaking term: $\dot{V}_a c_a$) and the fourth term for possible tracer coming in through leaks from the surrounding room or through the flushing ($\dot{V}_a c_a^0$).





OSD
11, 1643–1689, 2014



In the following sections, two different box model solutions, as used in this work for the low soluble tracers (water-side controlled: Sect. 2.2) and for the medium to high soluble tracers (air-side controlled: Sect. 2.3), are presented in detail. The simulated air/water concentration time series derived for a water (b and c in purple) and an air-side controlled (d and e in orange) tracer, are presented in Fig. 2. Three example wind speed conditions are assumed. The dashed lines indicate the change in wind speed and the grey background boxes the flushing periods.

## 2.2 Water-side controlled tracers

The following approach was used for tracers with relatively low solubility ($\alpha < 100$) for which the transfer velocity, $k_t$ is mainly restricted due to the water-side resistance. Here, a low solubility tracer is dissolved in the water volume which is considered well-mixed. High tracer concentration in the water and very low concentrations in the air ($c_a \simeq 0$) direct the flux from the water to the air (evasion).

Figure 2b, shows the simulated air-phase concentration time series of an example water-side controlled tracer at three example wind speed conditions (given in Fig. 2a, change of wind speed is denoted with grey dashed lines). Each condition starts with a closed air-space tank configuration (closed box – no flushing, see more details in Sect. 3.2.5) where the air-side concentration, starting from circa zero, increases linearly with time, due to the water-to-air gas exchange. At time $t_1$, the air-space is opened (open box – flushing on, flushing time is denoted with grey background) and a drastic decrease is observed due to dilution of the air-space concentration with the relatively clean ambient air entering the facility. As indicated in the figure, the higher the wind speed the faster the concentration increase. Figure 2c presents the water-phase concentration of the same tracer which in parallel starts from the highest concentration point and gradually decreases during the course of the experiment as more and more molecules escape the water to enter the gas-phase.

The ambient tracer concentration in the air entering the air-space through leaks or during flushing can be safely assumed as negligible in comparison to the levels used





OSD
11, 1643–1689, 2014



for all examined tracers. Omitting parameter $c_a^0$, simplifies the box model Eq. (1), which can be subsequently solved for $k_{tw}$ as follows:

$$k_{tw} = \frac{V_a}{A} \cdot \frac{\dot{c}_a + \lambda_{f,x} c_a}{c_w} \cdot \frac{1}{1 - \alpha c_a / c_w}, \quad (5)$$

where $\lambda_{f,x} = \dot{V}_a / V_a$ is the leak or flush rate for $x$ being 1 or 2, accordingly.

Applying Eq. (5), the instantaneous total transfer velocities ($k_{tw}$) can be calculated from time resolved measurements of air and water-side concentrations.

### 2.3 Air-side controlled tracers

In this approach, tracers with relatively high solubility ($\alpha > 100$) for which $k_t$ is expected to be controlled mainly by air-side processes, were used. Here, a relatively high soluble tracer is introduced with a constant flow to the air volume, continuously during the experiment. Due to low concentrations in the water volume, the net gas exchange flux is directed from the air to the water (invasion).

In Fig. 2d the air-phase concentration of an example air-side controlled tracer is shown. During the closed air-space period ($t_0$ to $t_1$), the concentration increases exponentially, as a fraction of the air-space molecules transmit into the water due to air-water gas exchange. At $t_1$, the concentration reaches a steady state, $SS_1$ where the input rate of the tracer is equal to the exchange rate between the two phases and the leak/flush rate.

At an equilibrium point, the concentration time derivative $\dot{c}_a$ is approximately zero so that Eq. (3) can be written as

$$c_a = \frac{\lambda_{ta} \frac{c_w}{\alpha} + \lambda^i c_a^i}{\lambda_{ta} + \lambda_{f,x}}, \quad (6)$$

where $\lambda_{ta} = \frac{A}{V_a} k_{ta}$ is the exchange rate and $\lambda^i = \frac{\dot{V}_a^i}{V_a}$ the input rate.





OSD
11, 1643–1689, 2014



After $SS_1$, the facility is flushed with ambient air (open air-space) and the concentration decreases abruptly. Under these conditions ($t_2$), a second steady state, $SS_2$ is developed at a lower concentration range. In $SS_1$, a very small leak rate is present ($\lambda_{f,1} \approx 0$, leak rate) while in $SS_2$ the leak rate is much larger due to the open air-space ($\lambda_{f,2}$, flush rate). Dividing the air-side concentrations of the two steady states $\frac{c_{a,1}}{c_{a,2}}$ (as given in Eq. 6) and solving it with respect to the exchange rate, yields

$$\lambda_{ta} = \frac{\lambda_{f,2} c_{a,2} - \lambda_{f,1} c_{a,1}}{(c_{a,1} - c_{a,2})}. \quad (7)$$

The total transfer velocities in the wind-wave tank box are calculated from

$$k_{ta} = \frac{\lambda_{ta} V_a}{A}. \quad (8)$$

### 2.3.1 Leak and flush rate

In most wind-wave facilities, small air leaks are inevitable. The amount of tracer escaping the air-space of the facility needs to be monitored and corrected for, as described in Sects. 2.2 and 2.3. To measure the leak/flush rate $\lambda_{f,x}$ for the open and closed configuration of the wind-wave tank, a non-soluble tracer (here $CF_4$) called a leak test gas, is used. Directly after closing the wind-wave tank, a small amount of the leak test gas is injected rapidly into the air-space. As the leak test gas is non-soluble, the water-side concentration $c_w$ as well as the gas exchange velocity $k_{ta}$ in Eq. (3) are equal to zero, reducing the air-side mass balance equation to

$$V_a \dot{c}_a = \dot{V}_a^i c_a^i - \dot{V}_a c_a. \quad (9)$$

After the initial injection, the input term $\dot{V}_a^i c_a^i$ in Eq. (9) vanishes, yielding $V_a \dot{c}_a = -\dot{V}_a c_a$. This simple differential equation can be solved easily to

$$c_a(t) = c_a(0) \cdot \exp(-\lambda_{f,x} \cdot t), \quad (10)$$





OSD
11, 1643–1689, 2014



where $c_a(0)$ is the concentration directly after the input of the leak test gas. Monitoring the concentration of the leak test gas over time and fitting an exponentially decreasing curve to this concentration time series, yields the leak/flush rate $\lambda_{f,x}$ of the system. In the "Aeolotron" facility, typical leak and flush rates were in the order of 0.05 to 0.4 $h^{-1}$ and 20 to 50 $h^{-1}$, accordingly.

## 3 Experiments

### 3.1 The "Aeolotron" wind-wave tank

The air-water gas exchange experiments were conducted in the large scale annular "Aeolotron" wind-wave tank at the University of Heidelberg, Germany (Fig. 3). With an outer diameter of 10 m, a total height of 2.4 m and a typical water volume of 18 000 L, the "Aeolotron" represents the world's largest operational ring shaped facility. The chamber is mostly gastight, thermally isolated, chemically clean and inert. In Fig. 3, a list of the main dimensions along with an aerial illustration of the facility are given. The tank is divided in 16 segments and an inner window extending through segments 16 to 4 allows visual access to the wind formed waves. The facility ventilation system consists of two pipes through which the air-space can be flushed with ambient air at a rate up to 50 $h^{-1}$. Two diametrically positioned ceiling mounted axial ventilators (segment 4 and 12) are used to generate wind velocities up to $u_{ref}$ = 12 m $s^{-1}$.

In the facility, several ambient parameters are monitored. Temperature measurements are provided by two temperature sensors (PT-100) installed in the water and air-phase of segment 15 (at heights of 0.5 m and 2.3 m, respectively). On the ceiling of the same segment a fan-anemometer (STS 020 by Greisinger electronic GmbH) installed in the center line, determines the wind velocity. Two humidity sensors are mounted in segments 2 and 13. An optical ruler provides the water height using the principle of comunicating vessels. Segments 1 and 11 contain the tracer inlets for the air and water phase accordingly. The leak test gas is introduced in segment 11.





OSD
11, 1643–1689, 2014



The annular geometry of the wind-wave tank, contrary to a linear geometry, permits homogeneous wave fields and unlimited fetch. The well mixed air-space (at few centimeters height above the surface) ensures no concentration gradients and therefore concentration measurements independent of the sampling height. On the other hand, the restricted size of the facility which leads off waves being reflected to the walls, results to a different wave field than on the open ocean.

### 3.2 Tracers and instrumentation

A series of 14 tracers covering a wide solubility ($\alpha = 0.4$ to 5470) and diffusivity ($Sc_w = 594$ to 1194) range, were selected for this study. Many of these tracers are very common in the ocean environment while the rest are used to extend the solubility and diffusivity ranges, a significant criterion for further physical investigations of the gas exchange mechanisms. Table 1 gives an overview of the examined tracers, with their respective molecular masses, solubility and Schmidt numbers, Sc (the dimensionless ratio of the kinematic viscosity of water $v$ and the diffusivity of the tracer $D$, $Sc = v/D$) at 20 °C.

All tracers were monitored on-line in both the air and the water-phase. The VOC measurements were performed using Proton Reaction Mass Spectrometry (PTR-MS) from Ionicon Analytik GmbH (Innsbruck, Austria) while for the halocarbons and $N_2O$, two Fourier Transform Infrared (FT-IR) Spectrometers (Thermo Nicolet iS10) were used. As leak test gas, carbon tetrafluoride ($CF_4$) was used. It was also measured by FT-IR spectrometry.

For the surfactant experiments, the soluble substance Triton X-100, $C_{14}H_{22}O(C_2H_4O)_{9.5}$ (Dow Chemicals, listed $M_r = 647\,g\,mol^{-1}$) was used to cover the water surface. Triton X-100 was chosen because of its common use as a reference substance to quantify the surface activity of unknown surfactant mixtures found in the open ocean (Frew et al., 1995a; Cosovic and Vojvodic, 1998; Wurl et al., 2011).

The operation and sampling conditions for both phases are briefly described below. Additional instrumentation for substantial supplementary measurements follows.





OSD
11, 1643–1689, 2014



### 3.2.1 Water-phase measurements

In the water-phase a PTR-Quadrupole-MS (water inlet in segment 3) and a FT-IR spectrometer (water inlet in segment 6) were used to measure the concentration levels of the VOCs and the halocarbons and $N_2O$, respectively. Our instrumentation, which is normally suited only for air sampling, was combined with an external membrane equilibrator (the oxygenator "Quadrox" manufactured by Maquet GmbH, Rastatt, Germany) to establish equilibrium between the water concentration and the gas stream to be measured. In this way, water-side concentrations could be obtained and used for the calculation of the transfer velocities for the low solubility tracers (see Sect. 2.2).

**Membrane equilibrator configuration**

The membrane equilibrator device includes a thin gas permeable membrane capable of separating the gas from the liquid phase (commercially available and often used in medicine as a human lung replacement to oxygenate blood). Water from the "Aeolotron" is constantly pumped through the membrane device where gas exchange occurs, due to the partial pressure difference of the gases involved, until equilibrium between air and water is achieved (Henry's law at constant temperature).

A detailed configuration of the membrane set-up in conjunction with the PTR-MS is shown in Fig. 6. The system consists of a water and an air loop, both constantly in contact with the membrane equilibrator. The dark blue lines represent the water loop where water was being pumped from the "Aeolotron" through the membrane and back into the facility, with a constant flow of 3.4 L min$^{-1}$. The light orange colored lines represent the air loop which has a link to the PTRQ-MS instrument. A synthetic air inlet and an excess flow exhaust are used to regulate the flow inside the air loop constant at 1 L min$^{-1}$ and the systems pressure at 1013 hPa. Part of the air that comes out of the equilibrator is driven to the PTRQ-MS for analysis, while the rest remains in the loop. The relative humidity in the equilibrated air increases after passing through the





OSD
11, 1643–1689, 2014



equilibrator, therefore the air tubing was heated to a few degrees above room temperature avoiding water condensation.

A similar set-up using a second membrane equilibrator was connected to the FT-IR instrument. The water flow was kept at a rate of about 3 L $min^{-1}$. Here the instrument's measuring cell was integrated into the air loop, removing the need for sample extraction, a synthetic air inlet and an exhaust. The air was circulated in the closed loop at a rate of approximately 150 mL $min^{-1}$. Between the equilibrator and the measuring cell a dehumidifying unit containing phosphorous pentoxide was used to remove water from the air stream and in this way protect the optical windows of the IR measuring cell.

The time constant of the membrane equilibrator was evaluated as described in Krall and Jähne (2014), providing a very fast response of $\simeq$ 1 min.

### PTRQ-MS configuration

The PTR-MS detection technique has been described in detail elsewhere (Lindinger et al., 1998). The instrument's ion source produces an excess of primary ions ($H_3O^+$) which then undergo proton transfer reactions with the VOC molecules of the air sample (sampling flow: 30 mL $min^{-1}$). Throughout the measurements, the drift pressure was kept to 2.1 mbar and the drift voltage at 600 V resulting to a field intensity (E/N) of 130 Td (Td = $10^{-17}$ $cm^2$ V $molecule^{-1}$).The SEV detector detected single ions with a dwell time of 1 s. During the experiments, 30 masses were monitored sequentially leading to a time resolution of 30 s. Possible mass overlapping was prevented by the careful reselection of the analysed compounds based on the initial mass scan.

At high humidity levels, as was the case here, a significant number of primary ions react with the water molecules of the sampled air forming water clusters (De Gouw and Warneke, 2007). This complicates the determination of the instruments sensitivity for some species (Jobson and McCoskey, 2010), and therefore calibrations were performed at the same humidity levels as present in the experiments and exactly the same measuring set-up (see Fig. 6) was used. Known concentrations of low-solubility VOCs were diluted in deionized water and then introduced into the water-phase of the





OSD
11, 1643–1689, 2014



facility, in precise volume quantities. To avoid losses of the investigated tracers into the air-phase due to air-water gas exchange, the water surface was covered with a large amount of an organic surfactant (0.446 mg $L^{-1}$, Triton X-100) and calm wind conditions were used to gently mix the air-space. Under such conditions gas exchange velocities were estimated to be negligible. Linear behavior was established for all low solubility tracers (dimensionless solubility < 20) examined at concentration levels between 0 and 7 µmol $L^{-1}$.

**FT-IR configuration**

The key aspects of Fourier-Transform Infrared spectroscopy, or FT-IR spectroscopy, are described in detail in Griffiths (2007). In this study, a Nicolet iS10 (manufactured by Thermo Fischer Scientific Inc., Waltham, MA., USA) FT-IR spectrometer with a custom made measuring cell of approximately 5 cm length was used. About every 5 s, one infrared absorbance spectrum with wavenumbers between 4000 $cm^{-1}$ and 650 $cm^{-1}$ with a resolution of 0.214 $cm^{-1}$ was acquired. Six of these single spectra were averaged to minimize noise and stored for further evaluation, leading to a time resolution of about 1 spectrum every 30 s. These spectra were later converted to concentrations by first scaling reference spectra of all tracers used in height to best represent the measured spectra, and then using a calibration to calculate the concentration from the scaling factors. This procedure, as well as the estimation of the uncertainties in the concentration measurements is described in detail in Krall (2013).

### 3.2.2 Air-phase measurements

In the air-phase, a PTR-Time of Flight (ToF)-MS (inlet in segment 3) with a time resolution of 10 s provided very fast on-line measurements for the VOCs while a FT-IR (inlet in segment 2) with a time resolution of 30 s was in parallel monitoring the halocarbons and $N_2O$. High time resolution measurements enabled a fast experimental procedure and at the same time high accuracy data analysis. Additionally, due to the fast on-line





OSD
11, 1643–1689, 2014



measurements, the transient response of the system could be followed very efficiently throughout the experimental procedure. Example air-side measurements are shown in Fig. 5 for a water and an air-side controlled tracer.

### PTR-TOF-MS configuration

The ionization principle of the PTR-TOF-MS is the same as the PTRQ-MS, however, here a Time of Flight mass spectrometer is used. Protonated VOC ions are driven through a transfer lens system to the pulse extraction region of the TOF-MS where they are accelerated and detected according to their flight times. In this way, higher time and mass resolutions are achieved (Jordan et al., 2009; Graus et al., 2010).

Throughout the measurements, the PTR-TOF-MS was configured in the standard V mode with a mass resolution of approximately 3700 m $\Delta$ m$^{-1}$. The drift voltage was maintained at 600 V and the drift pressure at 2.20 mbar (E/N 140 Td). Mass spectra were collected over the range 10–200 m z$^{-1}$ and averaged every 10 s, providing a mean internal signal for each compound. After acquisition all spectrum files were mass calibrated using $(H_2O)H^+$, $NO^+$ and $(C_3H_6O)H^+$ ions to correct for mass peak shifting. For the data processing software from Ionicon and Tofwerk (MID Calculator and TOF-DaqViewer) was used.

Calibrations in the air-phase were conducted under high humidity conditions equivalent to the sampling conditions during the experiments (85–90 % rel. humidity). The desired mixing ratios (1–600 ppbv) were obtained by appropriate dilution of the multicomponent VOC gas standard with synthetic air. Linear response was established for all examined tracers.

Parallel calibrations of both PTR-MS instruments showed similar sensitivities, hence no sensitivity correction was applied.





OSD
11, 1643–1689, 2014



### FT-IR configuration

A second Thermo Scientific Nicolet iS10 FT-IR spectrometer was used to measure the air-side concentrations. The measuring cell with a folded light path of a total length of 2 m, was kept at a constant temperature of 35 °C using a Thermo Nicolet cell cover. Air from the "Aeolotron" was sampled at a rate of 150 $min^{-1}$ at segment 13. As with the water-side instrumentation, water vapor was removed before entering the measuring cell using phosphorous pentoxide. The spectrometer settings, data acquisition as well as data processing was identical to the water-side instrumentation, see Sect. 3.2.1.

### 3.2.3 Error analysis of $k_t$

The individual total transfer velocity uncertainties were calculated applying the propagation of error for uncertainties independent from each other to Eq. (5), for the $k_{tw}$ and Eqs. (7) and (8) for the $k_{ta}$ accordingly.

The concentration uncertainties for the PTR-MS measurements were calculated using the background noise and the calibration uncertainty of each examined tracer. Relatively low uncertainties were obtained for the air-phase concentration levels $SS_1$ and $SS_2$ ranging between 1–1.5 % and 1.5–2.5 %, accordingly. The water-phase concentration uncertainty, $\Delta c_w$ was estimated the same way and the uncertainties were between 6.5–8 % for the concentration ranges used.

The uncertainty of the concentration measurement with the FT-IR spectrometers was found to be concentration dependent. All concentration uncertainties lie below 4 % for the typical concentrations measured in the described experiments.

The individual uncertainties for the leak and flush rates of all conditions were in the order of 0.5 % and 1 % accordingly. Based on the geometrical parameters of the facility the surface area uncertainty was calculated to be approximately 2 % while a maximum of 3 % is estimated for the volume uncertainty. For the solubility values provided by literature, accurate uncertainty estimations are difficult. Here we assume a maximum uncertainty of 10 % for all literature sources.





OSD
11, 1643–1689, 2014



The overall estimated total transfer velocity uncertainties therefore ranged between 6–12 % and 6–20 % for the $k_{ta}$ and $k_{tw}$ values of all examined tracers, respectively.

### 3.2.4 Additional instrumentation

Supplementary measurements of wind driven, surface associated, physical parameters such as the mean square slope and the water-sided friction velocity, were additionally made in the "Aeolotron" wind-wave tank to enable further investigations of the physical mechanisms of air-water gas exchange.

The mean square slope measurements, reflecting the surface roughness conditions, were performed in parallel with the gas-exchange measurements using a color imaging slope gauge (CISG) installed in segment 13. The CISG device uses the refraction properties of light at the air-water boundary. A color coded light source was placed below the water while a camera observed the water surface from above. Using lenses to achieve a telecentric setup, a relationship between surface slope and the registered color can be determined. Errors are calculated from the statistical fluctuations of the individually measured mean square slope values. A more detailed description can be found in Rocholz (2008).

The water-sided friction velocity, $u_{*,w}$ measurements, expressing the shear stress created on the water interface, were accomplished at a later stage using the same setting of the wind generator and the same surfactant coverage of the water surface. The momentum balance method was used as described in Bopp (2011) and Nielsen (2004). To apply this method, the friction between the water and the walls needs to be measured first. This is done by monitoring the decrease of the velocity of the water bulk after switching off the wind. In a stationary equilibrium, that is characterized by an equality of the momentum input into the water by the wind and the momentum loss due to friction at the walls, the friction velocity $u_{*,w}$ can be calculated from the mean water velocity. The water velocity was measured using a three-axis Modular Acoustic Velocity Sensor (MAVS-3 manufactured by NOBSKA, Falmouth, MA, USA) installed in the center of the water channel in segment 4 of the "Aeolotron" at a water depth





OSD
11, 1643–1689, 2014



of around 50 cm. The uncertainty of the friction velocity measurements is calculated from the statistical fluctuations of the bulk water velocity measurement as well as the uncertainty in the friction parameter used in the momentum balance method. Both sources of error are described in detail in Bopp (2011). Subsequently, simple error propagation was used to derive the wind speed ($u_{10}$) uncertainty from the Smith and Banke (1975) empirical relationship (see Appendix B), the error of which is assumed to be negligible.

### 3.2.5 Experimental arrangement

The "Aeolotron" facility was filled to 1 m height ($\sim 18\,m^3$ water volume) with clean deionized water. Diluted aqueous mixtures of low solubility tracers were introduced into the water-phase of the facility a day prior to an experiment and homogeneity was achieved using two circulating pumps. Before the beginning of each experiment (for the clean water surface cases) the water surface was skimmed to clean off any possible surface contamination. To do this, a small barrier with a channel is mounted between the walls of the tank, perpendicular to the wind direction while the wind is turned on at a low wind speed ($u_{ref} \approx 3\,m\,s^{-1}$). The wind pushes the water surface over the barrier into the channel removing any surfactant. A pump continuously empties the channel and drains the water contaminated with surface active materials.

Individual gas-washing bottles containing highly soluble tracers in liquid form were purged with a controlled flow of clean air that swept the air-tracer gas mixture into the air-phase of the facility. The bottles were kept in a thermostatic bath at 20 °C throughout the experimental procedure.

At the beginning of each experiment, the first wind speed condition was applied while the flushing of the air-space was turned on (open air-space) in order to achieve a background point for all tracers. Thereafter, the flushing was turned off (closed air-space) and the tracer concentration (air and water-side controlled) started to increase (see more in Sect. 2.3). Immediately after turning off the flushing, the leak test gas was introduced into the air-space. After the steady state point ($SS_1$) for the air-side controlled





OSD
11, 1643–1689, 2014



tracers was approached, the air-space was flushed once more with ambient air and an abrupt concentration decrease was observed. The same process was repeated for eight different wind speed conditions, progressing from lower to higher values. In Fig. 4 a time series of the experimental conditions; wind speed, flushing periods and air and water tracer inputs, are schematically represented. The obtained air-sided concentration time series over the eight wind speed conditions for a water (a) and an air-sided (b) example tracer are given in Fig. 5.

The wind speed varied from very low values ($u_{ref} = 0.74\,m\,s^{-1}$, equivalent to $u_{10} = 0.79\,m\,s^{-1}$) up to higher ones ($u_{ref} = 8.26\,m\,s^{-1}$, equiv. $u_{10} = 14.6\,m\,s^{-1}$). At the very beginning of the experiment, hardly any surface movement was seen. As the experiment progressed, the first capillary waves became apparent and started breaking above $u_{ref} = 4.8\,m\,s^{-1}$. Reaching larger wavelengths, wave braking and bubble formation was observable only at the highest wind speed condition.

The experimental procedure described above was repeated four times at clean surface conditions for all tracers listed in Table 1. Three further repetitions were accomplished with a surfactant (Triton X-100) covered water surface. The surfactant concentration in the fifth repetition was $0.033\,mg\,L^{-1}$ while in the last two a larger amount of $0.167\,mg\,L^{-1}$ was used.

Despite the well reproduced experimental conditions, small variations between the repetitions were observed. Table 2 displays a mean value of the main measured parameters along with the standard deviation, expressing the extent of variability between the repetitions, of each case. For the last condition of the clean case only three repetitions are used to derive the mean values, as in repetition three the wind speed was accidentally set to the wrong value. Also in repetition two, the $\sigma_s^2$ values observed in conditions 4, 5, 6 were significantly lower and therefore omitted from the averaging. Here we assume that the water surface was probably insufficiently skimmed before the experiment or that surfactant material might have entered the facility during the flushing phases. In the low surfactant case (case 2), no $u_{*,w}$ measurements were performed. The low surfactant case $u_{*,w}$ values used for data plotting (Sect. 4.2) are interpolated





OSD
11, 1643–1689, 2014



between the clean and the heavy surfactant cases. In the higher surfactant case (case 3), the first condition was omitted for reasons of experimental simplicity while $\sigma_s^2$ are available only for one repetition.

## 4 Results

Total transfer velocities for the examined 14 tracers reported in Table 1, were derived in all conducted experiments. The obtained transfer velocities are consistent with the solubility scaling. Maintaining our focus on the methodology, in this work, two contrasting tracers at opposite ends of the solubility spectrum, $N_2O$ ($\alpha = 0.67$) anticipated as an only water-side controlled tracer (i.e $k_{tw} \sim k_w$) and $CH_3OH$ ($\alpha = 5293$) similarly anticipated as an only air-side controlled (i.e. $k_{ta} \sim k_a$), are presented in more detail. In this way, we intend a validation of the efficacy of the above described methods and apparatus and subsequently a comparison with previous air–sea gas exchange studies. A full investigation of the mechanisms influencing the gas-exchange transfer and their relationship to individual gases over a broad solubility range will be presented in separate publications.

### 4.1 Gas-exchange transfer velocities

In Figs. 7 and 8, we present the experimentally obtained $k_{tw}$ for $N_2O$ and the $k_{ta}$ for $CH_3OH$ as a function of $u_{*,w}$ for all clean water surface experiments. In both figures, square symbols are used to present the transfer velocities corresponding to repetition 1, circles for repetition 2, triangles for repetition 3 and diamonds for repetition 4. Vertical bars in light red give the individual transfer velocity uncertainty (see Sect. 3.2.3) and the horizontal bars the uncertainty of the $u_{*,w}$ measurements. Here, a mean value of the uncertainties as estimated by Bopp (2011) (approximately 12 %) was applied. The $u_{*,w}$ measurements were not conducted in parallel with the transfer velocity measurements but in a later experiment using similar conditions. Moreover, the conducted





OSD
11, 1643–1689, 2014



$u_{*,w}$ measurements did not cover very low wind speed conditions such as the one used for the measurement of the first transfer velocity point. An extension of the $u_{*,w}$-$u_{ref}$ relationship, as derived from the higher wind speed measurements, embraces a big uncertainty; therefore a total 30 % uncertainty was estimated for the first point.

Small variations between the transfer velocity values for the same condition extending the given uncertainty bars were occasionally observed. A more apparent example is the lower transfer velocity points (circles) at conditions 4, 5 and 6 which arise as a result of the lower $\sigma_s^2$ values observed in repetition 2 (as described in Sect. 3.2.5). This effect could be taken as an indication that only one physical parameter is not enough to effectively describe the complicated process of the air–sea gas exchange. As the experimental conditions used in the four repetitions were similar but not identical (see Table 2), a four replicate mean value calculation was avoided and instead a fit though all points is chosen (black dashed line). Despite the non-identical conditions, the transfer velocity values are reproducible.

As indicated in Fig. 7, the $k_{tw}$ increases nonlinearly with $u_{*,w}$. The correlation could be described as linear up to $u_{*,w} = 0.86\,\mathrm{cm\,s^{-1}}$ (equiv. $u_{10} = 7.3\,\mathrm{m\,s^{-1}}$) while above this point, a faster increase is observed. This sudden increase in the so far linear tendency can be attributed to various water surface effects, which are not going to be discussed here.

The air-sided transfer velocities $k_{ta}$ (Fig. 8) in contrast, increase linearly ($R^2 = 0.99$) with $u_{*,w}$ throughout the examined velocity range ($u_{*,w} = 0.07$–$2.06\,\mathrm{cm\,s^{-1}}$ equiv. $u_{10} = 0.8$–$14.6\,\mathrm{m\,s^{-1}}$). As it appears from Fig. 8, the first transfer velocity values of $CH_3OH$ (i.e. those at the lowest turbulent condition) are slightly underestimated relative to the linear trend ($\simeq 10\,\%$). This could be explained due to the inefficiently mixed air-space caused by the lower turbulence conditions applied.

Overall, the observed trends and transfer velocity magnitudes of both $k_{tw}$ and $k_{ta}$ are in good agreement with observations made by previous studies. A more detailed comparison with literature follows in Sect. 4.3.





OSD
11, 1643–1689, 2014



### 4.2 Effect of surfactants

After obtaining clear, reproducible transfer velocity trends for a clean water surface, the effect of a surfactant was evaluated using two different surfactant (Triton X-100) concentrations. As expected, the surfactant decrease the transfer velocity of the tracers and also the surface stress, $u_{*,w}$. In Fig. 9, the transfer velocities of all seven experiments are presented against $u_{*,w}$ for $N_2O$ and $CH_3OH$. The clean water surface results are given in red, the results obtained using 0.033 mg $L^{-1}$ Triton X-100 in green and the one using 0.167 mg $L^{-1}$ Triton X-100 in blue. In both cases, reduced transfer velocities were observed which became more prominent as the surfactant concentration increased. In addition, the surfactant decreased the transfer velocity best at low wind speeds, becoming ineffective under higher turbulent conditions.

The surfactant effect shows significant differences between the two contrasting tracers. In the case of $N_2O$, the effect extends up to a factor of three for the lower wind speed range and still remains around a factor of 1.5 at the higher examined wind speeds where waves, wave breaking and bubbles are present. The observed trend though shows that at higher wind speed regimes (above the studied regime) no surfactant effect would be seen. The surfactant effect in case of $CH_3OH$ is significantly weaker, as here the exchange is mainly controlled by the air-side boundary layer.

### 4.3 Comparison with previous studies

The gas transfer velocities of weakly soluble tracers has been extensively studied over the previous years. Numerous $k_w$ parameterizations are available, derived from experimental (laboratory and field) measurements as well as physical models. In Fig. 10, a selection of some representative, experimentally derived parameterizations (colored lines), are used for comparison with the $k_{tw}$ (here $k_{tw} \sim k_w$) measurements of $N_2O$ (red points). The transfer velocities are plotted against the wind speed at 10 m height, $u_{10}$.

Looking at the lower wind speed range (0.7 to 4 m $s^{-1}$) an obvious spread between the various $k_w$ predictions can be observed extending through more than two orders





OSD
11, 1643–1689, 2014



of magnitude. Transfer velocity measurements at the very low wind speed regions are difficult to conduct and therefore the extended fits based on higher wind speed ranges can lead to incorrect estimations. An evaluation of the previous studies though, is not the objective of this publication. Here, we aim to highlight the huge disagreement in the lower wind speed regime that leads to great uncertainty in the predicted $k_w$ values. The projected absolute quantity differences to the atmospheric budgets though are estimated to be small since the fluxes themselves are small. One target of this study was to tackle the challenging measurements at the low wind speed end in order to achieve a better indication of the corresponding gas-exchange behavior. The middle wind speed range seems to be well represented in all studies. At the higher wind speed range, a smaller spread was observed especially above 12 m s$^{-1}$. This spread, a little more than an order of two, can lead to great discrepancies in the atmospheric budgets of the related tracers as the corresponding transfer velocities are much larger there.

The transfer velocities obtained in this study, show a closer agreement with the Clark et al. (1994) parameterization apart from the first wind speed condition. There, our results agree better with Nightingale et al. (2000).

In contrast to the weakly soluble, high soluble tracers have received much less attention. In Fig. 11, the total transfer velocity measurements of $CH_3OH$ (here $k_{ta} \sim k_a$) are compared with some available tunnel (Liss, 1973; Mackay and Yeun, 1983, colored lines) and model (Duce et al., 1991; Jeffery et al., 2010 from COARE Algorithm Fairall et al., 2003, grey lines) $k_a$ parameterizations as well as a recent $CH_3OH$ field study (Yang, 2013, black line with triangles).

As indicated in Fig. 11, our results agree very well with the previous laboratory parameterizations lying nearer to Mackay and Yeun (1983). Here again the first transfer velocity point deviates, though an increase by the estimated 10 % would still not change this trend. We note that also in case of ka, the lower wind speed range of the other experimental studies, is covered by a fit extension based on transfer velocities obtained at higher wind speeds.





OSD
11, 1643–1689, 2014



The transfer velocity values provided by model and field studies are about 1.5 to 2 times lower than the ones deriving from the laboratory measurements. This is to be expected as these studies include an extra turbulent resistance in the air-space at 10 m height.

## 5 Conclusions

This study has demonstrated that the "Aeolotron" wind-wave tank in combination with the adopted box model methodology, experimental procedure and instrumentation are capable of generating reliable and reproducible gas transfer velocities for species spanning a wide range of solubilities. The molecules nitrous oxide and methanol have been used to exemplify the behavior of sparingly soluble and highly soluble species. These represent cases of a water-side and an air-side layer control, as described in Sect. 2. Small differences between the obtained transfer velocity values of the four repetitions of the clean case, indicate that various physical parameters should be taken into account in future parameterizations in order to produce better transfer velocity estimations. The complete dataset for all species (including the intermediate cases of both layer control) along with the available micro-scale surface property parameters, extending over a low to medium wind speed regime, can be used to generate a generalized parametrization for the total transfer velocity. The derivation of this expression, which will be invaluable to future modeling efforts, will be presented in a separate publication.

Particularly interesting are the effects on the gas transfer velocity induced by the addition of a surfactant. Despite the surface micro-layer being commonly present on the ocean, its effect on air–sea gas transfer is poorly understood and there is a paucity of data both from the laboratory and the field. The impact of the surfactant is markedly different on the two tracers shown here. A strong reducing effect (up to a factor of three) was observed for the water-side controlled tracer, $N_2O$ while in the case of $CH_3OH$, the surfactant showed a very weak impact.





OSD
11, 1643–1689, 2014



We maintain that it is important to monitor the transfer process in both the water (using water-side controlled tracers) and the air-phase layer (using air-side controlled tracers) in order to develop a true enduring and generally applicable model for air–sea gas transfer. The results produced here correspond reasonably well with previous expressions for $k_a$ and $k_w$. In case of $k_w$, at low wind speeds there is a wide spread in the literature values, with this study corresponding most closely with those of Clark et al. (1994) and Nightingale et al. (2000). At high wind speeds the previous parameterizations are divided into three groups and this study lies in the central group. Despite the relatively small number of investigations, in case of $k_a$, the literature spread is much smaller with our results nicely corresponding to the previous laboratory parameterizations (i.e. Liss, 1973; Mackay and Yeun, 1983).

This study, based on data from the world's largest annular wind-wave facility, derived from advanced analytical technology which has been set-up to monitor the gas concentration changes in both the air and the water-phase simultaneously at unprecedented measurement frequency, has proven to produce high quality transfer velocity measurements. On the basis of our results, we recommend the proposed methodology for future air–sea gas exchange measurements.

## Appendix A: Relationship between air-sided and water-sided variables

The experimentally calculated water-sided total transfer velocities, $k_{tw}$ were converted to the equivalent air-sided total transfer velocities, $k_{ta}$ using:

$$k_{ta} = \alpha k_{tw}. \quad \text{(A1)}$$

Air-sided friction velocities can be converted to water-sided friction velocities by

$$u_{*,w} = \sqrt{\frac{\rho_a}{\rho_w}} u_{*,a}. \quad \text{(A2)}$$





OSD
11, 1643–1689, 2014



## Appendix B: $u_{10}$ derivation using $u_{*,a}$

The wind speed at a height of 10 m, $u_{10}$ is calculated from its relationship with the air-sided friction velocity and the drag coefficient, $C_d$ using

$$C_d = \frac{u_{*,a}{}^2}{u_{10}^2} \quad \text{(B1)}$$

Here, the Smith and Banke (1975) empirical relationship between the drag coefficient and the wind speed was used

$$10^3 C_d = 0.63 + 0.066 u_{10} \quad \text{(B2)}$$

*Acknowledgements.* We own a special thank to J. Auld and T. Klüpfel for their valuable assistance and support during the gas exchage experiments. The mean square slope values were kindly provided by R. Rocholz. R. Sander is thanked for the helpful and insightful discussions on solubility matters considering this manuscript. Furthermore we thank all members of B. Jähne's group for their understanding and support during the measurements. We acknowledge the financial support of the BMBF Verbundprojekt SOPRAN www.sopran.pangaea.de; (SOPRAN grant 03F0611A, 03F0611K, 03F0611F and 03F0662F).

The service charges for this open access publication
have been covered by the Max Planck Society.

## References

Benkelberg, H. J., Hamm, S., and Warneck, P.: Henry's law coefficients for aqueous solutions of acetone, acetaldehyde and acetonitrile, and equilibrium constants for the addition compounds of acetone and acetaldehyde with bisulfite, J. Atmos. Chem., 20, 17–34, doi:10.1007/Bf01099916, 1995. 1674

Betterton, E. A. and Hoffmann, R. M.: Henry's law constants of some environmentally important aldehydes, Environ. Sci. Technol., 22, 1415–1418, doi:10.1021/Es00177a004, 1988. 1674





OSD
11, 1643–1689, 2014



Bopp, M: Messung der Schubspannungsgeschwindigkeit am Heidelberg Aeolotron mittels der Impulsbilanzmethode, Bachelor Thesis, University of Heidelberg, Germany, 2011. 1658, 1659, 1661

Broecker, W. S., Peng, T. H., Ostlund, G., and Stuiver, M.: The distribution of bomb radiocarbon in the ocean, J. Geophys. Res.-Oceans, 90, 6953–6970, doi:10.1029/Jc090ic04p06953, 1985. 1645

Carpenter, L. J., Archer, S. D., and Beale, R.: Ocean–atmosphere trace gas exchange, Chem. Soc. Rev., 41, 6473–6506, 2012. 1644

Clark, J. F., Wanninkhof, R., Schlosser, P., and Simpson, H. J.: Gas-exchange rates in the tidal Hudson River using a dual tracer technique, Tellus B, 46, 274–285, 1994. 1664, 1666, 1688

Cosovic, B. and Vojvodic, V.: Voltammetric analysis of surface active substances in natural seawater, Electroanalysis, 10, 429–434, doi:10.1002/(SICI)1521-4109(199805)10:6<429::AID-ELAN429>3.0.CO;2-7, 1998. 1652

Dacey, J. W. H., Wakeham, G. S., and Howes, L. B.: Henry's law constants for dimethylsulfide in freshwater and seawater, Geophys. Res. Lett., 11, 991–994, doi:10.1029/Gl011i010p00991, 1984. 1674

Danckwerts, P. V.: Significance of liquid-film coefficients in gas absorption, Ind. Eng. Chem., 43, 1460–1467, 1951. 1645

De Gouw, J. A. and Warneke, C.: Measurements of volatile organic compounds in the earth's atmosphere using proton-transfer-reaction mass spectrometry, Mass Spectrom. Rev., 26, 223–257, doi:10.1002/mas.20119, 2007. 1654

Donelan, M. A. and Wanninkhof, R.: Concepts and issues, in: Gas Transfer at Water Surfaces, 127, edited by: Donelan, M. A., Drennan, W. M., Saltzman, E. S., and Wanninkhof, R., American Geophysical Union, 1–10, 2002. 1644, 1645

Duce, R. A., Liss, P. S., Merrill, J. T., Atlas, E. L., Buat-Menard, P., Hicks, B. B., Miller, J. M., Prospero, J. M., Arimoto, R., Church, T. M., Ellis, W., Galloway, J. N., Hansen, L., Jickells, T. D., Knap, A. H., Reinhardt, K. H., Schneider, B., Soudine, A., Tokos, J. J., Tsunogai, S., Wollast, R., and Zhou, M.: The atmospheric input of trace species to the world ocean, Geophys. Res. Lett., 5, 193–259, doi:10.1029/91GB01778, 1991. 1664, 1689

Fairall, C. W., Bradley, E. F., Hare, J. E., Grachev, A. A., and Edson, J. B.: Bulk parameterization of air–sea fluxes: updates and verification for the COARE algorithm, J. Climate, 16, 571–591, doi:10.1175/1520-0442(2003)016<0571:BPOASF>2.0.CO;2, 2003. 1664





OSD
11, 1643–1689, 2014



Field, C. B., Behrenfeld, M. J., Randerson, J. T., and Falkowski, P.: Primary production of the biosphere, Science, 281, 237–240, 1998. 1644

Frew, N. M., Bock, E. J., McGillis, W. R., Karachintsev, A. V., Hara, T., Münsterer, T., and Jähne, B.: Variation of air–water gas transfer with wind stress and surface viscoelasticity, in: Air–water Gas Transfer, Selected Papers from the Third International Symposium on Air-Water Gas Transfer, edited by: Jähne, B. and Monahan, E. C., Aeon, Hanau, 529–541, 1995. 1652

Graus, M., Muller, M., and Hansel, A.: High resolution PTR-TOF: quantification and formula confirmation of VOC in real time, J. Am. Soc. Mass Spectr., 21, 1037–1044, doi:10.1016/j.jasms.2010.02.006, 2010. 1656

Griffiths, P. R.: Fourier Transform Infrared Spectrometry, 2nd Edn., Wiley Interscience, 2007. 1655

Ho, D. T., Law, C. S., Smith, M. J., Schlosser, P., Harvey, M., and Hill, P.: Measurements of air–sea gas exchange at high wind speeds in the Southern Ocean: implications for global parameterizations, Geophys. Res. Lett., 33, L16611, doi:10.1029/2006GL026817, 2006. 1688

Jähne, B.: Air–sea gas exchange, in: Encyclopedia Ocean Sciences, Elsevier, 3434–3444, 2009. 1645

Jähne, B. and Haussecker, H.: Air–water gas exchange, Annu. Rev. Fluid Mech., 30, 443–468, 1998. 1644, 1645, 1646

Jähne, B., Münnich, K. O., and Siegenthaler, U.: Measurements of gas-exchange and momentum-transfer in a circular wind-water tunnel, Tellus, 31, 321–329, 1979.

Jähne, B., Münnich, K. O., Bösinger, R., Dutzi, A., Huber, W., and Libner, P.: On the parameters influencing air–water gas-exchange, J. Geophys. Res.-Oceans, 92, 1937–1949, 1987.

Janini, G. M. and Quaddora, A. L.: Determination of activity coefficients of oxygenated hydrocarbons by liquid-liquid chromatography, J. Liq. Chromatogr., 9, 39–53, doi:10.1080/01483918608076621, 1986. 1674

Jeffery, C. D., Robinson, I. S., and Woolf, D. K.: Tuning a physically-based model of the air–sea gas transfer velocity, Ocean Model., 31, 28–35, doi:10.1016/j.ocemod.2009.09.001, 2010. 1664, 1689

Jobson, B. T. and McCoskey, J. K.: Sample drying to improve HCHO measurements by PTR-MS instruments: laboratory and field measurements, Atmos. Chem. Phys., 10, 1821–1835, doi:10.5194/acp-10-1821-2010, 2010. 1654





OSD
11, 1643–1689, 2014



Jordan, A., Haidacher, S., Hanel, G., Hartungen, E., Mark, L., Seehauser, H., Schottkowsky, R., Sulzer, P., and Mark, T. D.: A high resolution and high sensitivity proton-transferreaction time-of-flight mass spectrometer (PTR-TOF-MS), Int. J. Mass Spectrom., 286, 122–128, doi:10.1016/j.ijms.2009.07.005, 2009. 1656

Krall, K. E.: Laboratory Investigations of Air–Sea Gas Transfer under a Wide Range of Water Surface Conditions, Dissertation, University of Heidelberg, available at: http://www.ub.uni-heidelberg.de/archiv/14392 (last access: 18 June 2014), 2013. 1647, 1655, 1674, 1680

Krall, K. E. and Jähne, B.: First laboratory study of air–sea gas exchange at hurricane wind speeds, Ocean Sci., 10, 257–265, doi:10.5194/os-10-257-2014, 2014. 1654

Kräuter, C.: Aufteilung des Transferwiderstandes zwischen Luft und Wasser beim Austausch flüchtiger Substanzen mittlerer Löslichkeit zwischen Ozean und Atmosphäre, Diploma, University of Heidelberg, Germany, available at: http://www.ub.uni-heidelberg.de/archiv/13010 (last access: 18 June 2014), 2011 . 1647

Lewis, W. K. and Whitman, W. G.: Principles of gas absorption, Ind Eng. Chem., 16, 1215–1220, 1924.

Lindinger, W., Hansel, A., and Jordan, A.: On-line monitoring of volatile organic compounds at pptv levels by means of proton-transfer-reaction mass spectrometry (PTR-MS) – medical applications, food control and environmental research, Int. J. Mass. Spectrom., 173, 191–241, doi:10.1016/S0168-1176(97)00281-4, 1998. 1654

Liss, P. S.: Processes of gas-exchange across an air–water interface, Deep-Sea Res., 20, 221–238, 1973. 1664, 1666, 1689

Liss, P. S. and Merlivat, L.: Air–sea gas exchange rates: IIntroduction and synthesis, in: The Role of Air–Sea Exchange in Geochemical Cycling, Reidel, Boston, MA, 113–129, 1986. 1688

Liss, P. S. and Slater, P. G.: Flux of gases across air–sea interface, Nature, 247, 181–184, 1974. 1645

Mackay, D. and Yeun, A. T. K.: Mass-transfer coefficient correlations for volatilization of organic solutes from water, Environ. Sci. Technol., 17, 211–217, doi:10.1021/Es00110a006, 1983. 1664, 1666, 1689

McGillis, W. R., Edson, J. B., Ware, J. D., Dacey, J. W. H., Hare, J. E., Fairall, C. W., and Wanninkhof, R.: Carbon dioxide flux techniques performed during GasEx-98, Mar. Chem., 75, 267–280, doi:10.1016/S0304-4203(01)00042-1, 2001. 1688





OSD
11, 1643–1689, 2014



McGillis, W. R., Edson, J. B., Zappa, C. J., Ware, J. D., McKenna, S. P., Terray, E. A., Hare, J. E., Fairall, C. W., Drennan, W., Donelan, M., DeGrandpre, M. D., Wanninkhof, R., and Feely, R. A.: Air–sea $CO_2$ exchange in the equatorial Pacific, J. Geophys. Res.-Oceans, 109, C08S02, doi:10.1029/2003jc002256, 2004. 1688

Millet, D. B., Jacob, D. J., Custer, T. G., de Gouw, J. A., Goldstein, A. H., Karl, T., Singh, H. B., Sive, B. C., Talbot, R. W., Warneke, C., and Williams, J.: New constraints on terrestrial and oceanic sources of atmospheric methanol, Atmos. Chem. Phys., 8, 6887–6905, doi:10.5194/acp-8-6887-2008, 2008. 1644

Millet, D. B., Guenther, A., Siegel, D. A., Nelson, N. B., Singh, H. B., de Gouw, J. A., Warneke, C., Williams, J., Eerdekens, G., Sinha, V., Karl, T., Flocke, F., Apel, E., Riemer, D. D., Palmer, P. I., and Barkley, M.: Global atmospheric budget of acetaldehyde: 3-D model analysis and constraints from in-situ and satellite observations, Atmos. Chem. Phys., 10, 3405–3425, doi:10.5194/acp-10-3405-2010, 2010. 1644

Nielsen, R.: Gasaustausch – Entwicklung und Ergebnis eines schnellen Massenbilanzverfahrens zur Messung der Austauschparameter, Dissertation, University of Heidelberg, available at: http://www.ub.uni-heidelberg.de/archiv/5032 (last access: 18 June 2014), 2004. 1658

Nightingale, P. D.: Air–sea gas exchange. lower atmosphere processes, in: Surface Ocean, edited by: Quéré, C. L. and Saltzman, E. S., AGU Books Board, 69–97, 2009. 1645

Nightingale, P. D., Malin, G., Law, C. S., Watson, A. J., Liss, P. S., Liddicoat, M. I., Boutin, J., and Upstill-Goddard, R. C.: In situ evaluation of air–sea gas exchange parameterization using novel conservation and volatile tracers, Global Biogeochem. Cy., 14, 373–387, 2000. 1664, 1666, 1688

Pozzer, A., Jöckel, P., Sander, R., Williams, J., Ganzeveld, L., and Lelieveld, J.: Technical Note: The MESSy-submodel AIRSEA calculating the air–sea exchange of chemical species, Atmos. Chem. Phys., 6, 5435–5444, doi:10.5194/acp-6-5435-2006, 2006. 1644

Robbins, G. A., Wang, V., and Stuart, D. J.: Using the headspace method to determine Henry's law constants, Anal. Chem., 65, 3113–3118, doi:10.1021/Ac00069a026, 1993. 1674

Rocholz, R.: Spatiotemporal Measurement of Short Wind-Driven Water Waves, Dissertation, University of Heidelberg, available at: http://www.ub.uni-heidelberg.de/archiv/8897 (last access: 18 June 2014), 2008. 1658

Saltzman, E.: Introduction to surface ocean–lower atmosphere processes, in: Surface Ocean-Lower Atmosphere Processes, Geophysical Research Series, 187, 2009. 1644





OSD
11, 1643–1689, 2014



Sander, R.: Compilation of Henry's Law Constants for Inorganic and Organic Species of Potential Importance in Environmental Chemistry (Version 3), available at: http://www.henrys-law.org (last access: 18 June 2014), 1999. 1674

Schaffer, D. L. and Daubert, E. T.: Gas-liquid chromatographic determination of solution properties of oxygenated compounds in water, Anal. Chem., 286, 1585–1589, 1969. 1674

Shahin, U. M., Holsen, T. M., and Odabasi, M.: Dry deposition measured with a water surface sampler: a comparison to modeled results, Atmos. Environ., 36, 3267–3276, doi:10.1016/S1352-2310(02)00315-1, 2002.

Smith, S. D. and Banke, E. G.: Variation of sea-surface drag coefficient with wind speed, Q. J. Roy. Meteor. Soc., 101, 665–673, 1975. 1659, 1667, 1689

Snider, J. R. and Dawson, A. G.: Tropospheric light alcohols, carbonyls, and acetonitrile: concentrations in the southwestern United States and Henry's law data, J. Geophys. Res., 90, 3797–3805, doi:10.1029/Jd090id02p03797, 1985. 1674

Staudinger, J., and Roberts, V. P.: A critical review of Henry's law constants for environmental applications, Crit. Rev. Env. Sci. Tec., 26, 205–297, 1996.

Tsai, W.-T. and Liu, K.-K.: An assessment of the effect of sea surface surfactant on global atmosphere–ocean $CO_2$ flux, J. Geophys. Res.-Oceans, 108, 3127–3142, 2003.

Wanninkhof, R.: Relationship between wind-speed and gas-exchange over the ocean, J. Geophys. Res.-Oceans, 97, 7373–7382, 1992.

Wanninkhof, R. and McGillis, W. R.: A cubic relationship between air–sea $CO_2$ exchange and wind speed, Geophys. Res. Lett., 26, 1889–1892, doi:10.1029/1999gl900363, 1999. 1688

Wanninkhof, R., Asher, W., Weppernig, R., Chen, H., Schlosser, P., Langdon, C., and Sambrotto, R.: Gas transfer experiment on Georges Bank using 2 volatile deliberate tracers, J. Geophys. Res.-Oceans, 98, 20237–20248, 1993. 1645

Wanninkhof, R., Asher, W. E., Ho, D. T., Sweeney, C., McGillis, W. R.: Advances in quantifying air–sea gas exchange and environmental forcing, Annu. Rev. Mar. Sci., 1, 213–244, 2009. 1645, 1688

Watson, A. J., Upstill-Goddard, R. C., and Liss, P. S.: Air sea gas-exchange in rough and stormy seas measured by a dual-tracer technique, Nature, 349, 145–147, 1991. 1645

Weiss, R. F. and Price, B. A.: Nitrous oxide solubility in water and seawater, Mar. Chem., 8, 347–359, doi:10.1016/0304-4203(80)90024-9, 1980. 1674





OSD
11, 1643–1689, 2014



Williams, J., Holzinger, R., Gros, V., Xu, X., Atlas, E., and Wallace, D. W. R.: Measurements of organic species in air and seawaater from the tropical Atlantic, Geophys. Res. Lett., 31, L23S06, doi:10.1029/2004GL020012, 2004. 1644

Wurl, O., Wurl, E., Miller, L., Johnson, K., and Vagle, S.: Formation and global distribution of sea-surface microlayers, Biogeosciences, 8, 121–135, doi:10.5194/bg-8-121-2011, 2011. 1652

Yang, M., Nightingale, P. D., Beale, R., Liss, P. S., Blomquist, B., and Fairall, C.: Atmospheric deposition of methanol over the Atlantic Ocean, P. Natl. Acad. Sci. USA, 110, 20034–20039, doi:10.1073/pnas.1317840110, 2013. 1664, 1689

Yaws, C. L.: Handbook of Transport Property Data, Gulf Publishing Company, 1995. 1674

Yaws, C. L. and Pan, X.: Liquid heat-capacity for 300 organics, Chem. Eng.-New York, 99, 130–134, 1992. 1674





OSD
11, 1643–1689, 2014



**Table 1.** Molecular masses ($M$ in g mol$^{-1}$), dimensionless solubility ($\alpha$) and Schmidt numbers in air ($Sc_a$) and water ($Sc_w$) for the investigated tracers at 20 °C.

| Gas | Formula | $M$ | $\alpha$ | $Sc_a^{12}$ | $Sc_w^{12}$ |
|---|---|---|---|---|---|
| methanol | $CH_3OH$ | 32.04 | 5293 [1] | 1.0268 | 671.04 |
| 1-butanol | $C_4H_9OH$ | 74.12 | 4712 [2] | 1.8198 | 1141.7 |
| acetonitrile | $CH_3CN$ | 41.05 | 1609 [3] | 1.2957 | 832.07 |
| acetone | $(CH_3)_2CO$ | 58.08 | 878.0 [3] | 1.4921 | 880.53 |
| 2-butanone | $C_2H_5COCH_3$ | 72.11 | 598.9 [2] | 1.7344 | 1159.8 |
| acetaldehyde | $CH_3CHO$ | 44.05 | 378.7 [4] | 1.0786 | 824.90 |
| ethyl acetate | $CH_3C(O)OC_2H_5$ | 88.10 | 156.4 [5] | 1.8183 | 997.46 |
| dms | $CH_3SCH_3$ | 62.13 | 16.62 [6] | 1.4484 | 979.40 |
| benzene | $C_6H_6$ | 78.11 | 5.672 [7] | 1.6785 | 980.46 |
| toluene | $C_6H_5CH_3$ | 92.14 | 4.529 [7] | 1.8409 | 1176.3 |
| trifluoromethane | $CHF_3$ | 70.01 | 0.760 [8] | 1.2132 | 747.50 |
| nitrous oxide | $N_2O$ | 44.01 | 0.676 [9] | 1.0007 | 593.90 |
| isoprene | $C_5H_8$ | 68.12 | 0.31 [10]–0.69 [11,*] | 1.6617 | 1193.9 |
| pentafluoroethane | $CF_3CHF_2$ | 120.0 | 0.415 [8] | 1.5106 | 1027.0 |

[1] Schaffer and Daubert (1969), [2] Snider and Dawson (1985), [3] Benkelberg et al. (1995), [4] Betterton and Hoffmann (1988), [5] Janini and Quaddora (1986), [6] Dacey et al. (1984), [7] Robbins et al. (1993), [8] Krall (2013), [9] Weiss and Price (1980), [10] Yaws and Pan (1992), [11] Sander (1999), [12] Yaws (1995). * only available values at 25 °C.





OSD
11, 1643–1689, 2014



**Table 2.** Reference velocities, $u_{ref}$ (m s$^{-1}$), friction velocities, $u_{*,w}$ (cm s$^{-1}$), mean square slope, $\sigma_s^2$, air temperature, $t_a$ (°C), water temperature, $t_w$ (°C) mean values and % standard deviations, as quantified in the "Aeolotron" facility for 1: clean surface experiments, 2: surface covered with 0.033 mg L$^{-1}$ Triton X-100, 3: surface covered with 0.167 mg L$^{-1}$ Triton X-100.

| Case | Parameter | cond.1 | cond.2 | cond.3 | cond.4 | cond.5 | cond.6 | cond.7 | cond.8 |
|---|---|---|---|---|---|---|---|---|---|
| | $u_{ref}$ (±%) | 0.744 (1.3) | 1.421 (0.5) | 2.052 (0.3) | 2.674 (0.5) | 3.621 (0.1) | 4.805 (0.3) | 6.465 (0.2) | 8.256 (0.1) |
| | $u_{*,w}$ (±%) | 0.071 (1.5) | 0.156 (0.7) | 0.251 (0.4) | 0.361 (0.6) | 0.559 (0.2) | 0.856 (0.6) | 1.369 (0.3) | 2.048 (0.1) |
| 1 | $\sigma_s^2$ (±%) | 0.002 (1.7) | 0.007 (1.4) | 0.013 (1.2) | 0.016 (0.5) | 0.024 (2.2) | 0.046 (2.0) | 0.078 (3.0) | 0.118 (6.3) |
| (×4) | $t_a$ (±%) | 21.29 (1.5) | 21.18 (1.5) | 21.09 (1.6) | 20.99 (1.6) | 20.88 (1.6) | 20.75 (1.6) | 20.59 (1.7) | 20.50 (1.8) |
| | $t_w$ (±%) | 19.30 (1.7) | 19.37 (1.8) | 19.41 (1.8) | 19.41 (1.8) | 19.39 (1.8) | 19.34 (1.9) | 19.29 (2.0) | 19.26 (2.1) |
| | $u_{ref}$ (±%) | 0.800 (–) | 1.460 (–) | 2.091 (–) | 2.717 (–) | 3.650 (–) | 4.851 (–) | 6.502 (–) | 8.288 (–) |
| | $u_{*,w}$ (±%) | – | – | – | – | – | – | – | – |
| 2 | $\sigma_s^2$ (±%) | 0.002 (–) | 0.002 (–) | 0.002 (–) | 0.008 (–) | 0.010 (–) | 0.020 (–) | 0.071 (–) | 0.111 (–) |
| (×1) | $t_a$ (±%) | 22.11 (–) | 22.04 (–) | 21.94 (–) | 21.77 (–) | 21.64 (–) | 21.44 (–) | 21.19 (–) | 21.11 (–) |
| | $t_w$ (±%) | 19.80 (–) | 19.88 (–) | 19.93 (–) | 19.93 (–) | 19.93 (–) | 19.90 (–) | 19.88 (–) | 19.85 (–) |
| | $u_{ref}$ (±%) | – | 1.451 (1.2) | 2.075 (0.0) | 2.707 (0.6) | 3.667 (0.3) | 4.913 (0.4) | 6.615 (0.2) | 8.371 (0.0) |
| | $u_{*,w}$ (±%) | – | 0.105 (1.7) | 0.175 (0.1) | 0.260 (0.9) | 0.421 (0.4) | 0.680 (0.7) | 1.132 (0.4) | 1.713 (0.0) |
| 3 | $\sigma_s^2$ (±%) | – | 0.002 (–) | 0.002 (–) | 0.002 (–) | 0.005 (–) | 0.007 (–) | 0.040 (–) | 0.096 (–) |
| (×2) | $t_a$ (±%) | – | 21.51 (1.4) | 21.59 (1.3) | 21.60 (1.0) | 21.53 (0.9) | 21.51 (0.6) | 21.34 (0.7) | 21.22 (0.9) |
| | $t_w$ (±%) | – | 19.83 (0.5) | 19.86 (0.6) | 19.90 (0.7) | 19.94 (0.6) | 19.95 (0.7) | 19.95 (0.7) | 19.95 (0.7) |





OSD
11, 1643–1689, 2014



**Table C1.** Naming conventions.

| | |
|---|---|
| $k_w$ | transfer velocity in water for a water-sided viewer |
| $k_a$ | transfer velocity in air for an air-sided viewer |
| $k_{tw}$ | total transfer velocity for a water-sided viewer |
| $k_{ta}$ | total transfer velocity for an air-sided viewer |
| $c_w$ | water-side concentration |
| $c_a$ | air-side concentration |
| $V_w$ | water volume |
| $V_a$ | air volume |
| $A$ | water surface |
| $\lambda_{f,1}$ | leak rate |
| $\lambda_{f,2}$ | flush rate |
| $\alpha = \frac{c_w}{c_a}$ | dimensionless solubility |
| $Sc_w$ | Schmidt number in water |
| $Sc_a$ | Schmidt number in air |
| $M$ | molecular mass |
| $u_{*,w}$ | water-sided friction velocity |
| $u_{*,a}$ | air-sided friction velocity |
| $\rho_w$ | density of water |
| $\rho_a$ | density of air |
| $u_{ref}$ | reference wind speed |
| $\sigma_s^2$ | mean square slope |
| $u_{10}$ | wind speed at 10 m height |





OSD
11, 1643–1689, 2014



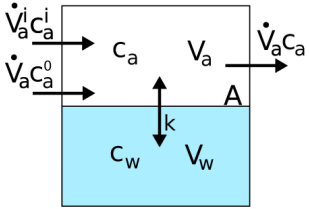


**Figure 1.** Mass balances for the air and water-side. Naming convention is as follows: $A$: water surface area; $V_a$: air volume; $V_w$: water volume; $k$: gas transfer velocity, $c_a$: air-side concentration; $c_w$: water-side concentration; $c_a^i$: input tracer concentration; $c_a^0$: tracer concentration in the ambient air. The dotting denotes the time derivative of the related symbol.





OSD
11, 1643–1689, 2014



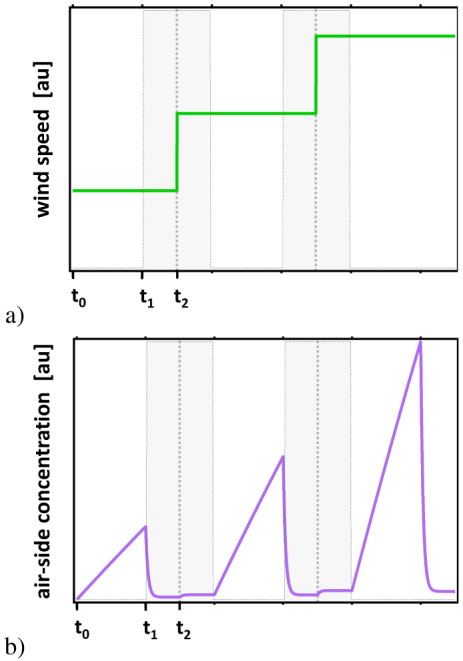


**Figure 2.** Simulated concentration time series for a water (**b** and **c**) and an air-side controlled (**d** and **e**) tracer in both air and water-phase, at three example wind speed conditions. The gray background denotes the air-phase flashing periods and the dashed lines the change of the wind speed condition. $SS_1$ and $SS_2$ mark the developed steady states.





OSD
11, 1643–1689, 2014



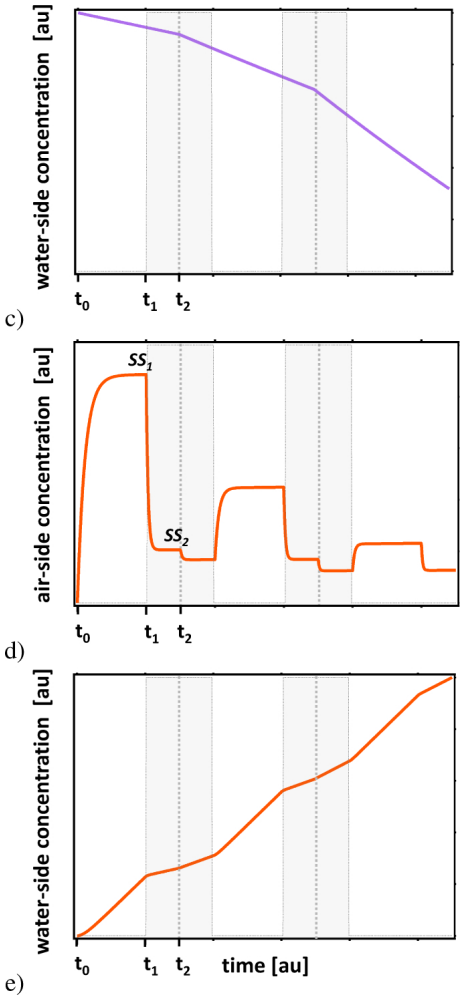


**Figure 2.** Continued.





OSD
11, 1643–1689, 2014



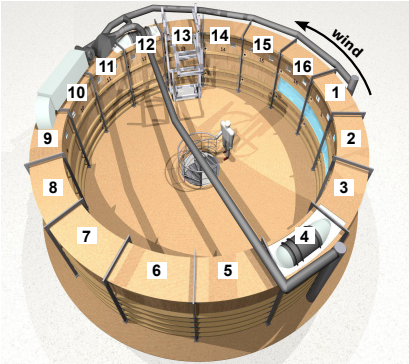


| Main Features | |
|---|---|
| mean circumference | 29.2 m |
| mean diameter | 9.3 m |
| mean width | 61 cm |
| mean total height | 241 cm |
| typical water depth | 100 cm |
| surface area | 17.9 $m^2$ |
| typical water volume | 17.9 $m^3$ |
| typical air volume | 24.4 $m^3$ |

**Figure 3.** An aerial illustration of the "Aeolotron" tank and its main features. The numbers denote the segments. The axial fans producing the wind can be seen in the roof of segments 4 and 12. The air pipes supplying fresh air and removing waste air are shown in grey (Figure adapted from Krall, 2013).





OSD
11, 1643–1689, 2014



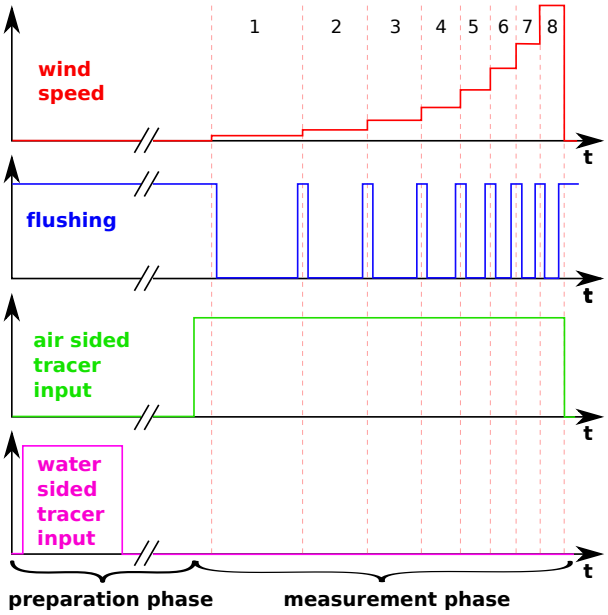


**Figure 4.** Schematic time series of the wind speed, flushing periods and air/water tracer inputs.





OSD
11, 1643–1689, 2014



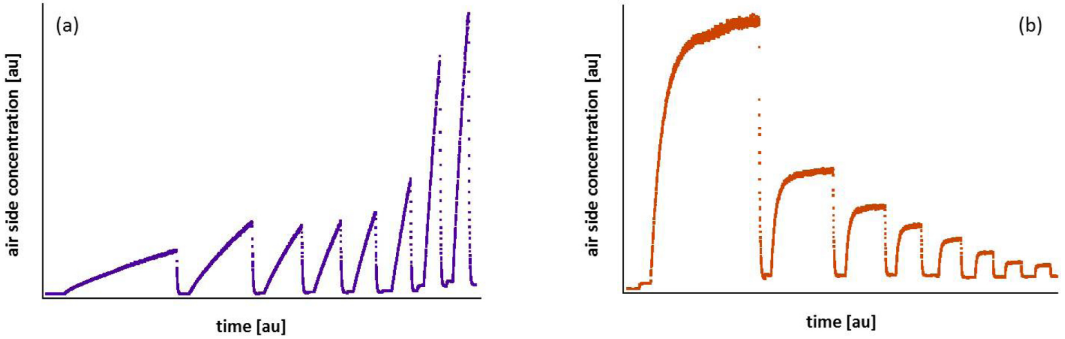


**Figure 5.** Air-side concentrations obtained for an example water-side **(a)** and an air-side **(b)** controlled tracer through-out the experimental procedure.





OSD
11, 1643–1689, 2014



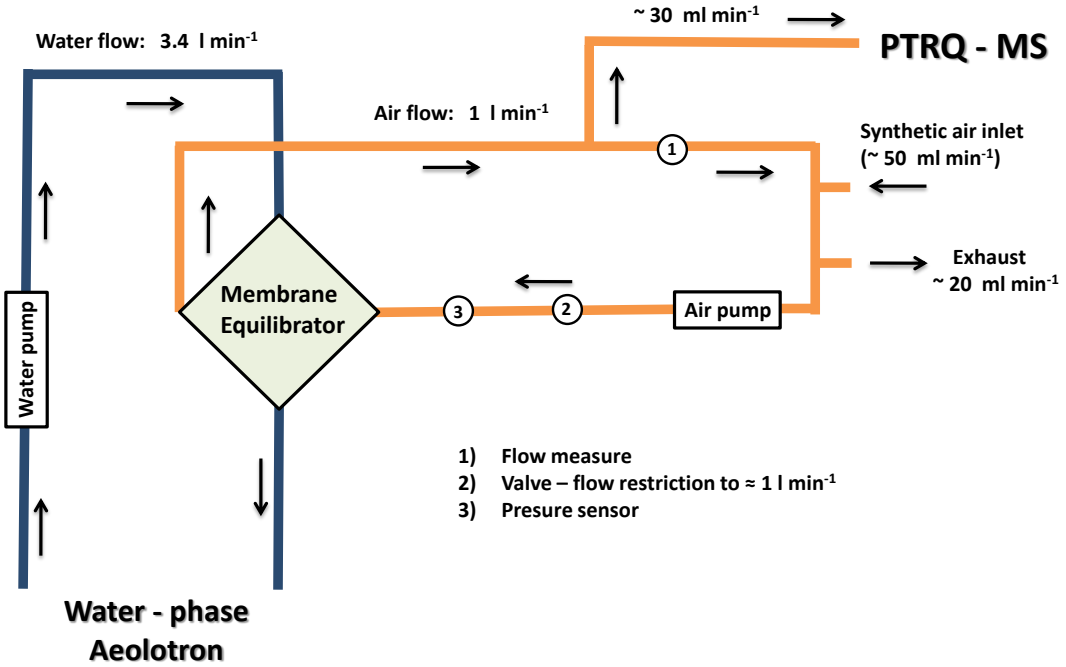


**Figure 6.** "Membrane equilibrator – PTRQ-MS" set-up schematic. The dark blue and orange lines represent the water and air loops of the system, accordingly.





OSD
11, 1643–1689, 2014



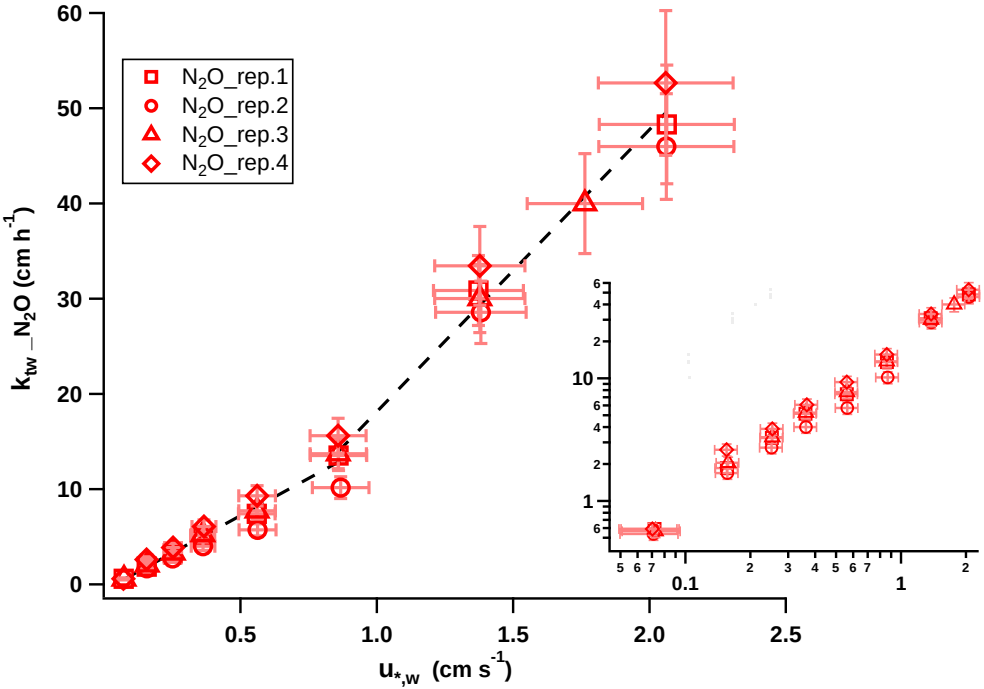


**Figure 7.** Total transfer velocity of $N_2O$ of four clean case repetitions plotted against $u_{*,w}$.





OSD
11, 1643–1689, 2014



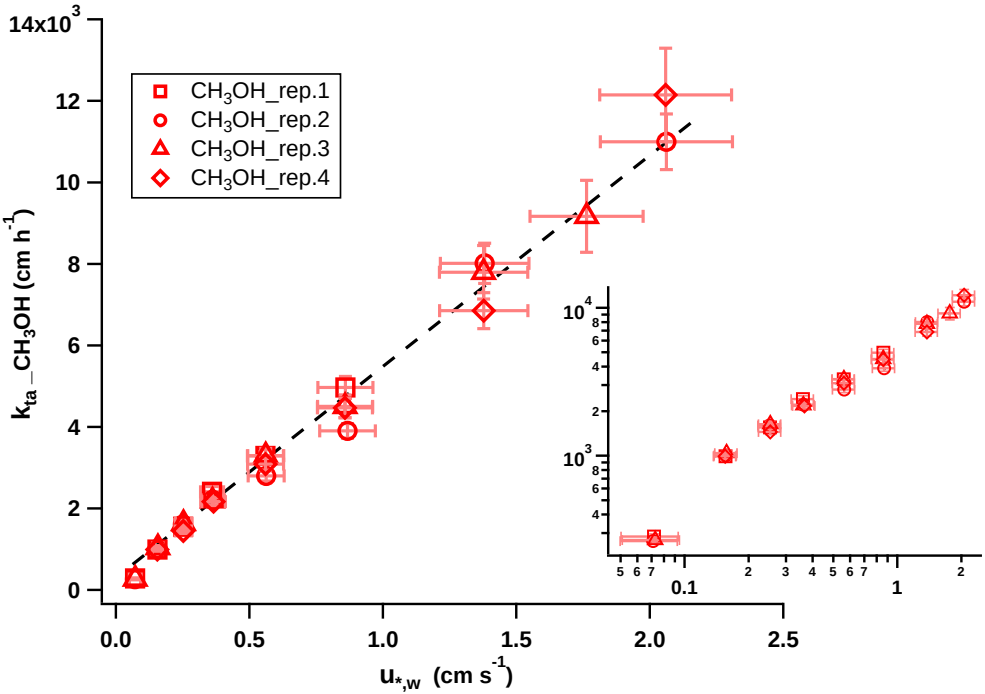


**Figure 8.** Total transfer velocity of $CH_3OH$ of four clean case repetitions plotted against $u_{*,w}$.





OSD
11, 1643–1689, 2014



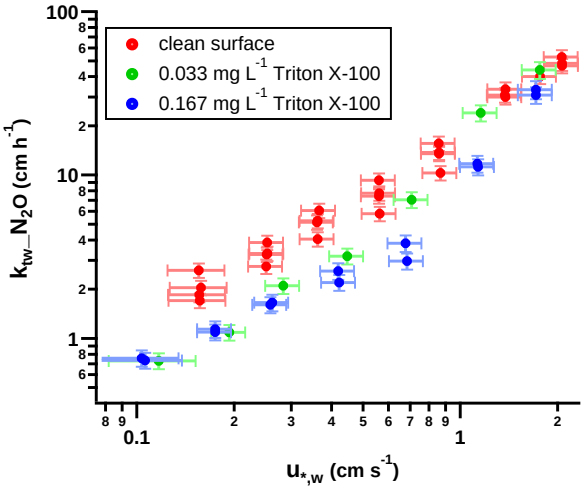


a)

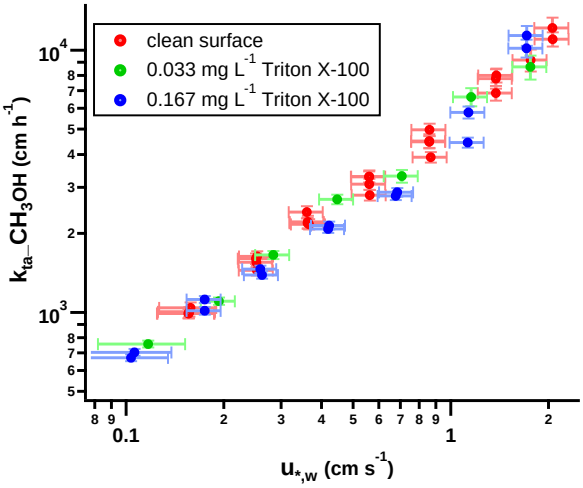


b)





OSD
11, 1643–1689, 2014

Gas exchange in the Lab

E. Mesarchaki et al.



**Figure 9.** Effect of the two different surfactant concentrations on the total transfer velocities of **(a)** $N_2O$ and **(b)** $CH_3OH$.





OSD
11, 1643–1689, 2014



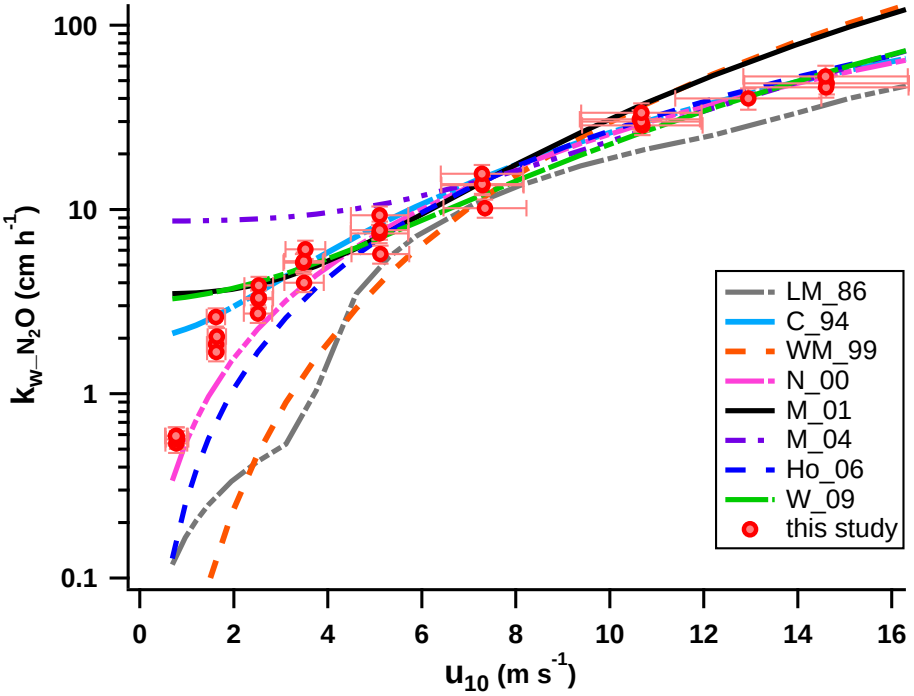


**Figure 10.** Comparison between the $N_2O$ measurements of this study (red circles) and previous $k_w$ parameterizations. The colored lines corespond to: LM_86: Liss and Merlivat (1986), C_94: Clark et al. (1994), WM_99: Wanninkhof and McGillis (1999), N_00: Nightingale et al. (2000), M_01: McGillis et al. (2001), M_04: McGillis et al. (2004), Ho_06: Ho et al. (2006), and W_09: Wanninkhof et al. (2009).





OSD
11, 1643–1689, 2014



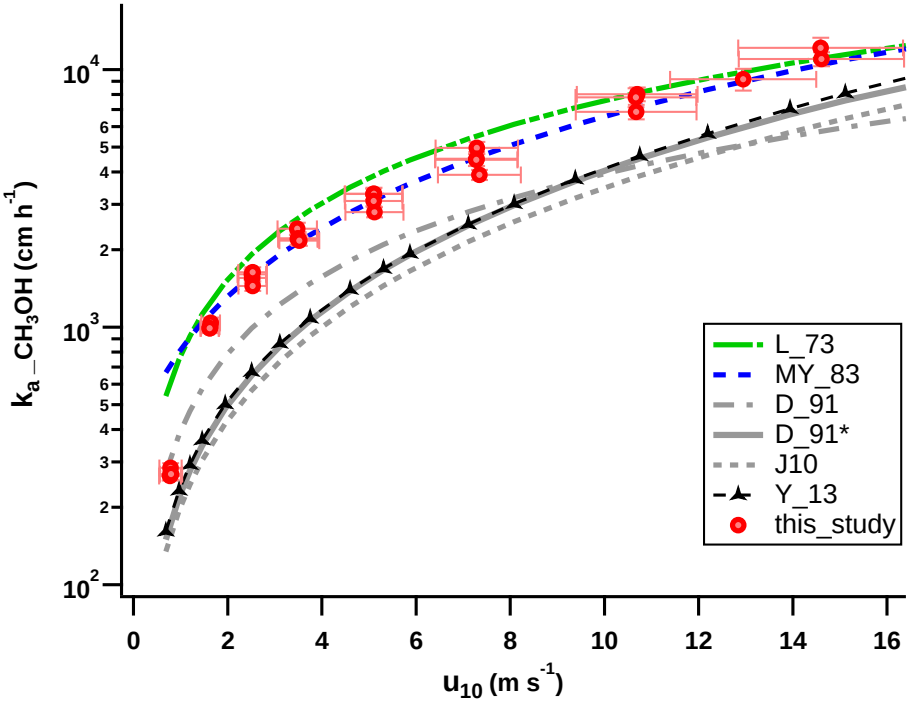


**Figure 11.** Comparison between the $CH_3OH$ measurements of this study (red circles) and previous $k_a$ parameterizations. Experimental studies are presented with colored lines: L_73: Liss (1973), MY_83: Mackay and Yeun (1983) and Y_13: Yang (2013) while model studies are given with grey lines: D_91 using the MW, D_91* using the $Sc_a$: Duce et al. (1991) and J_10: Jeffery et al. (2010) using a Smith and Banke (1975) derived drag coefficient term.





OSD
11, 1643–1689, 2014